



HAL
open science

Experimental evidence of the metastability of ferric smectite

Fabien Baron, Sabine Petit, Alain Decarreau

► **To cite this version:**

Fabien Baron, Sabine Petit, Alain Decarreau. Experimental evidence of the metastability of ferric smectite. *Geochimica et Cosmochimica Acta*, 2019, 265, pp.69-84. 10.1016/j.gca.2019.08.040 . hal-02363221

HAL Id: hal-02363221

<https://cnrs.hal.science/hal-02363221v1>

Submitted on 3 Dec 2020

HAL is a multi-disciplinary open access archive for the deposit and dissemination of scientific research documents, whether they are published or not. The documents may come from teaching and research institutions in France or abroad, or from public or private research centers.

L'archive ouverte pluridisciplinaire **HAL**, est destinée au dépôt et à la diffusion de documents scientifiques de niveau recherche, publiés ou non, émanant des établissements d'enseignement et de recherche français ou étrangers, des laboratoires publics ou privés.

Experimental evidence of the metastability of ferric smectite

Fabien Baron^{1,2,*}, Sabine Petit¹, and Alain Decarreau¹

¹Institut de Chimie des Milieux et Matériaux de Poitiers - IC2MP, UMR CNRS 7285, Université de Poitiers, 86022 Poitiers, France

²Laboratoire de Planétologie et Géodynamique - LPG, UMR CNRS 6112, Université de Nantes, 44300 Nantes, France

*corresponding author: Fabien Baron - fabien.baron@univ-poitiers.fr

Abstract

The stability of clay minerals, and especially ferric smectites, as a function of time, is of interest for natural environments due to their high capacity to exchange electrons that control a large part of the geochemical cycle of different redox-sensitive organic or inorganic compounds (e.g., elements, nutrients, pollutants). An experimental approach based on hydrothermal synthesis was performed for synthesizing two series of iron-rich smectite (Na-nontronite) at two pH (near 12 and 13) from 1 day to several months at 150 °C. XRD, FTIR, and HRTEM data of the synthetic products confirmed the formation of Na-nontronite for the short time duration experiments. However, the dissolution of Na-nontronite and the concomitant formation of aegirine were observed with the increase of synthesis time. The pH of crystallization fluids clearly influences the rate of the reactions. At highest pH, Na-nontronite disappeared totally after two months and aegirine and hematite were the only crystalline phases observed. The chemical compositions of solutions were over time far from the thermodynamic stability field of nontronite, but very close to that of the aegirine-hematite equilibrium, suggesting that the formation of the nontronite depends on kinetics. The formation of nanoparticulate Na-nontronite at the earlier stage of the experiments appears likely due to their specific thermodynamic properties linked to the nanoscale particle size (i.e., high surface energy and high hydration properties). However, Na-nontronites dissolve when they reach a critical size, leading to the formation of the stable assemblage aegirine and hematite.

Keywords: smectite metastability, nontronite, nanoparticle, synthesis, clay minerals, thermodynamic equilibrium

32

33 **1 Introduction**

34 The thermodynamic stability of clay minerals and especially smectites has been abundantly debated
35 for several decades and remains an ongoing question. The stability field of smectites and their
36 response to a biogeochemical constraint appear today a crucial point due to (i) their ubiquitous
37 presence in earth surface/near-surface systems (Wilson, 2013), (ii) their important role in mineral-
38 solution-life-atmosphere interactions, and (iii) their large use in chemistry and geotechnical
39 applications (e.g. engineering barrier).

40 Lippmann (1982, 1979, 1977) and Eberl (1978) were among the first ones to point out the potential
41 metastability or the unstability of clay minerals, especially smectites, illites, and interstratified
42 illite-smectites, under Earth surface and subsurface conditions. These authors concluded from
43 thermodynamic approaches and natural observations that the chemical formation field of these clay
44 minerals is located far from their thermodynamic equilibrium, indicating that their formation is
45 derived by kinetics reactions. This interpretation was supported by the fine grain size of the clay
46 minerals. Lippmann (1982) proposed that clay minerals owe their existence and their varied
47 properties not to equilibrium thermodynamic properties, but to kinetics inhibitions inherent to Earth
48 surface-subsurface conditions and to their heterogeneous chemistry. May et al. (1986) failed to
49 determine equilibrium solubility for smectites during dissolution experiments because the
50 compositions of contact solutions are controlled by the formation of other mineral phases. These
51 authors, as Lippmann (1982), concluded that smectites are not true equilibrium phases due to their
52 heterogeneous nature, but persist in natural environments for kinetic reasons. By contrast, the
53 agreement between predicted equilibria and experimental solubility studies involving smectites
54 obtained by Kittrick (1971a, 1971b, 1971c), and Kittrick and Peryea (1989, 1988) could indicate,
55 at least, a metastable equilibrium. The integration of different solubility studies involving chlorites,
56 smectites, and illites allowed Aja and Rosenberg (1992) to conclude that clay minerals having
57 variable compositions are true phases capable to attain equilibrium. Essene and Peacor (1995) then
58 called this thermodynamic status into question, leading to an intense debate between Aja and
59 Rosenberg (1996) and Essene and Peacor (1997). However, the latter authors favored clay minerals
60 sequences occurring through the Ostwald's step rules (e.g., smectite to illite reaction via
61 interstratified illite-smectite), but diverged for the irreversibility or reversibility of these clay
62 minerals sequences at low temperatures. Ostwald's step rules state that the first precipitated phase

63 is usually not the thermodynamically stable phase but rather a metastable phase (Ostwald, 1897).
64 Several discussions on Ostwald's step rules were found in the literature (see Nývlt, 1995 and
65 references therein), including formation kinetic rates between metastable and stable phases (e.g.,
66 Morse and Casey, 1988), irreversible thermodynamics involving minimization of entropy
67 production (e.g., Van Santen, 1984), or change of the solution structure (Nývlt, 1995). The
68 metastability of smectite thus remains an open question, notably because very few studies were
69 conducted to determine this status using mineral synthesis experiments.

70 Nontronite appears a good smectite candidate to discuss this question because it presents the
71 advantage of being easily synthesized with a controlled crystal-chemistry in a simple chemical
72 system (see review in Petit et al., 2017 and references therein). Nontronite is the ferric iron [Fe(III)]
73 end-member of the dioctahedral smectite group. The dominant octahedral cation is Fe(III), but
74 some Mg or Al are also commonly present in the octahedral sheet of natural nontronite (Fig. 1).
75 The layer charge of nontronite is mainly tetrahedral and comes from R(III) for Si tetrahedral
76 substitutions (R(III) being Al(III) and possibly Fe(III)). Nontronite originates from a large diversity
77 of surface-subsurface environments at the surface of the Earth (e.g., Wilson, 2013). Fe-bearing
78 smectites are also an important redox buffer in the subsurface environments affecting the
79 biogeochemical cycles of elements, nutrients, and pollutants (Neumann et al., 2011; Stucki et al.,
80 1988; Stucki, 2013). Fe-rich smectites are also widespread at the surface of Mars (Poulet et al.,
81 2005; Mustard et al., 2008; Carter et al., 2013; Carter et al., 2015; Michalski et al., 2015), but the
82 actual crystal chemistry and the origin of these smectites are still debated and remain an open
83 question.

84 Nontronite is largely used in diverse applications such as in degradation or retention of organic
85 compounds, reduction of the mobility of heavy metals, or potentially used for geological disposal
86 of high-level nuclear waste (see review in Petit et al., 2017 and references therein). The use of
87 nontronite in environmental applications implies that nontronite must be stable for a long period at
88 the human scale. The stability field and the evolution of nontronite over time are consequently
89 important questions.

90 The objectives of the present study are to study the metastability of nontronite by evidencing
91 mineralogical and crystal-chemical reactions involving nontronite as a function of time and to
92 determine if the metastability of nontronite is only due to its large chemical heterogeneity. To
93 address these questions, mineral synthesis experiments were conducted from 1 day to several

94 months at 150 °C using the simplest Na-Fe(III)-Si-O-OH chemical system. Full characterization
95 of synthetic products was made to show the potential mineralogical reactions over time. The
96 solution in contact with synthetic products was also analyzed to highlight the evolution of the
97 physico-chemical parameters variations induced by mineralogical reactions. Thermodynamic
98 calculations were also performed to determine the stability field of nontronite and to assess the
99 reaction pathway.

100

101 **2 Materials and methods**

102 **2.1 Synthesis of Fe(III)-nontronites**

103 Fe(III)-nontronites were synthesized from a co-precipitated gel having a Fe/Si of 0.73 according to
104 the procedure described in Baron et al. (2016). Two series of Fe(III)-nontronites were synthesized
105 at 150 °C under equilibrium vapor pressure using Teflon[®] metallic-coated hydrothermal reactors
106 (Parr[®], reactor number: 4744). The powdered gel precursor (0.5 g) was placed in contact with 30
107 mL of NaOH solutions at 0.01 M concentration for the first series (pH_i = 12) and at 0.15 M
108 concentration for the second series (pH_i = 13.3) (Table 1). For both series, syntheses were
109 performed for 1, 15, 31, 62, and 183 days. The 6 days samples were taken from Baron et al. (2016).
110 A temperature of 150 °C was chosen according to Decarreau et al. (2008, 2004), to obtain Fe(III)-
111 nontronites with the best crystallinity and prevent, theoretically, the crystallization of aegirine.
112 Moreover, a synthesis temperature of 150 °C can be considered suitable to extrapolate with
113 temperatures of clay minerals formation at the Earth surface (Petit et al., 2017). After the
114 hydrothermal treatment, solid materials were collected by filtration (<0.1 μm) and crushed in agate
115 mortar after a drying step of 24 hrs at 45 °C. The volume of experimental solutions decreased
116 linearly as a function of synthesis time due to some small uncontrolled leaks. The lost volume
117 followed this relation: $V_{\text{lost}} \text{ (mL)} = -0.044 \times N_{\text{day}} + 29.92$ ($R^2 = 0.99$) with V_{lost} = volume of lost
118 water and N_{day} = number of days.

119

120 **2.2 Characterization of the synthetic materials**

121 A Jeol 2100 UHR (LaB₆) transmission electron microscope at 200 kV equipped with an Energy
122 Dispersive X-ray Spectrometer (EDS) was used for High-Resolution Transmission Electron
123 Microscopy (HRTEM) and Transmission electron microscopy (TEM) observations. For

124 observations, samples were dispersed in deionized water using sonication. A droplet of the
125 suspension was then placed on a TEM copper grid and dried at ambient temperature.

126 Mid-infrared (MIR) spectra were obtained using a Magna-IR 760 Nicolet spectrometer equipped
127 with an Ever-Glo source, a KBr beam splitter, and a DTGS-KBr detector. MIR spectra resulted
128 from the average of 100 scans acquired in transmission mode over the 400 - 4000 cm^{-1} range with
129 a resolution of 4 cm^{-1} . For analyses, KBr pellets were obtained by mixing 1 mg of powdered
130 samples with 150 mg of KBr, and pressed at 8 kbar and then dried at 110 °C.

131 Powder X-ray diffraction (XRD) patterns were recorded using a Bruker D8 advance diffractometer
132 equipped with a $\text{CuK}\alpha$ radiation, a tension of 40 kV and a current of 40 mA. Over the 2 - 57 °2 θ
133 range, a step size of 0.025 °2 θ and a counting time of 0.6 s were used. For the (06.33) reflection, a
134 step size of 0.025 °2 θ and a counting time of 0.6 s were used over the 57 - 63 °2 θ range.

135

136 **2.3 Characterization of the experimental solutions**

137 The pH of the starting solutions (pH_i) and the pH of solutions at the end of syntheses (pH_f) were
138 measured at 25 °C with a FiveEasy™ Mettler Toledo (pH +/- 0.04) calibrated with three buffer
139 solutions at pH 7.01, 10.14 and 12.00 (Table 1).

140 The total aqueous Si concentrations of the solutions at the end of the synthesis were measured using
141 the molybdenum blue method from Strickland and Parsons (1972), using a Jenway 6300
142 spectrophotometer setting at 820 nm (Table 1). The solutions recovered by filtration (<0.1 μm) at
143 the end of the synthesis were diluted in Milli-Q® pure water (18 M Ω .cm) to measure the total
144 aqueous Si concentrations in the linear range of the calibration curve. Total aqueous sodium (Na)
145 concentration was measured from filtrated <0.1 μm solutions using atomic absorption spectroscopy
146 (AAS) with a Varian® AA240FS spectrometer (Table 1). Solutions were diluted in 2 wt. % HNO_3
147 to measure aqueous concentrations in the linear range of the calibration curve (i.e. from 8.26×10^{-6}
148 to 4.35×10^{-5} mol·L⁻¹). Solutions were prepared in KNO_3 solution with a final concentration of
149 0.05 mol·L⁻¹ to reduce the Na ionization in the flame during measurements.

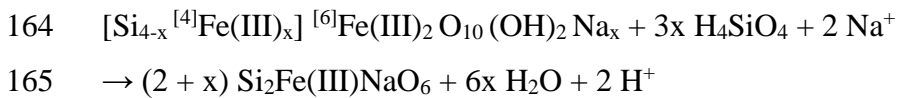
150

151 **2.4 Thermodynamic calculations**

152 Activities of H^+ , Na^+ (aq), and H_4SiO_4 (aq) for the different syntheses were calculated at 150 °C from
153 chemical analyses using Phreeqc® software (Parkhurst and Appelo, 2013) associated with the
154 thermodem database (thermodem.brgm.fr) (Table 2). Thermodynamic data of aegirine and

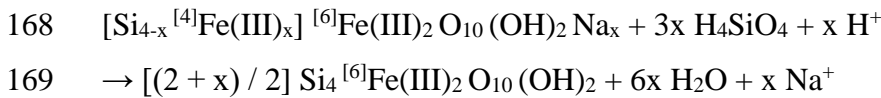
155 hematite were taken from Robie and Hemingway (1995) and Hemingway (1990), respectively
 156 (included in the thermoddem database) (Table 3). Thermodynamic data of nontronites and
 157 ferripyrophyllite were obtained using the prediction model of thermodynamic properties of clay
 158 minerals developed by Blanc et al. (2015) and added in the thermoddem database (Table 3). The
 159 stability fields of nontronite ($[\text{Si}_{4-x}^{[4]}\text{Fe(III)}_x]^{[6]}\text{Fe(III)}_2 \text{O}_{10}(\text{OH})_2 \text{Na}_x$) with different $^{[4]}\text{Fe(III)}$
 160 content ($x = 0.5, 0.75, 1.15$ and 1.35), aegirine ($\text{Si}_2\text{Fe(III)NaO}_6$), hematite (Fe_2O_3), and
 161 ferripyrophyllite ($\text{Si}_4^{[6]}\text{Fe(III)}_2 \text{O}_{10}(\text{OH})_2$) were calculated at 150°C and assuming a constant
 162 activity of water using the six following equilibrium reactions:

163 nontronite - aegirine



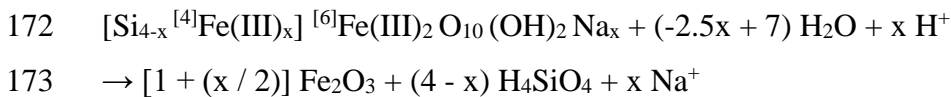
166

167 nontronite - ferripyrophyllite



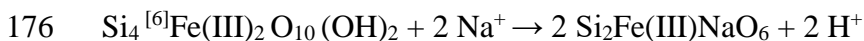
170

171 nontronite - hematite



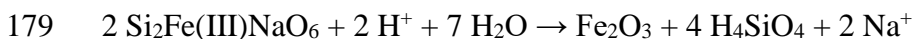
174

175 ferripyrophyllite - aegirine



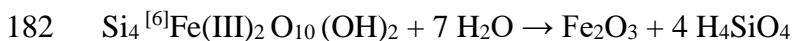
177

178 aegirine - hematite



180

181 ferripyrophyllite - hematite



183

184 For the six reactions, Fe was treated as an inert compound in the sense of Thompson (1955) on the
185 basis of the lack of dissolved Fe in solutions (see below). The $^{54}\text{Fe(III)}$ contents (x) of nontronites
186 were fixed taking into account the structural formula of the synthesized nontronites.

187

188 **3 Results**

189 **3.1 Chemical properties of solutions**

190 The evolution of pH_i , pH_f and total aqueous concentrations of Si and Na with time are given in
191 Table 1. For all syntheses (except sample NT35) the pH_f values are always lower than pH_i values.
192 This trend is linked to the consumption of OH groups during the dissolution of the gel precursor
193 and the precipitation of hydroxylated minerals (Decarreau, 1985). The total aqueous concentration
194 of Fe was assumed to be in the same order as in Baron et al. (2016); i.e., at least two orders of
195 magnitude lower than those of Na and Si.

196

197 **3.2 Characterization of solid materials**

198 **3.2.1 Starting gel**

199 The XRD pattern of the gel precursor exhibits: i) a broad reflection at 13.6 \AA , that could be due to
200 the occurrence of some TOT-like layers (Decarreau et al., 2008); ii) a clear increase in the overall
201 diffracted intensities around 30° (2θ) characterizing the high proportion of poorly organized
202 material (Figs. 2 and 3). The MIR spectrum of the gel precursor has similarities with that of
203 synthesized nontronite (Fig. 4). In the OH stretching (ν) region ($3700 - 3200 \text{ cm}^{-1}$), a shoulder is
204 observed at 3555 cm^{-1} and corresponds to the 3560 cm^{-1} band attributed to $\nu \text{ Fe}^{3+}_2\text{-OH}$ vibrations
205 as for the crystallized nontronite (see below). The broad band at 3400 cm^{-1} is attributed to large
206 amounts of adsorbed water (Fig. 4). In the $1200\text{-}400 \text{ cm}^{-1}$ region, the broad bands observed for the
207 gel appear at the same wavenumbers ranges as for the synthesized nontronite (Fig. 4). Thus, IR and
208 XRD data suggest the occurrence of TOT-like structures in the gel precursor. Layered structures
209 could not be identified from HRTEM observations which reveal aggregates composed of rounded
210 particles (Fig. 5a), that rather exhibit an amorphous state (Fig. 5b).

211

212 **3.2.2 Nontronite series synthesized at $\text{pH}_i = 12$**

213 Powder XRD patterns of samples exhibit reflections at 12.59 \AA (001), 4.58 \AA (02-11), 3.11 \AA (004),
214 2.62 \AA (13-20), and $1.528 - 1.537 \text{ \AA}$ (06,33) (Fig. 2) corresponding to Na-nontronite (Brindley and

215 Brown, 1980; Decarreau et al., 2008). No other crystalline material has been identified in any
216 samples. The shift of the (06,33) reflection from 1.528 Å (1, 6, 15 days samples) to 1.537 Å (62,183
217 days samples) reflects the increase in total Fe(III) content in the smectite structure (Eggleton, 1977;
218 Brigatti, 1983; Köster et al., 1999; Heuser et al., 2013; Petit et al., 2015), and more precisely, for
219 strictly Fe(III)-synthesized nontronites, the increase in the amount of Fe(III) - for - Si(IV)
220 tetrahedral substitutions (Petit et al., 2015; Baron et al., 2016) (Fig. 2b). The apparent full width at
221 half-maximum (FWHM) of the (001) reflection (c^* axis) and the (06, 33) one (ab plane) decreases
222 with synthesis time (Fig. 2b) due to, respectively, an increase in the number of regularly stacked
223 layers and a better crystallinity in the layer plane of nontronite particles.

224 MIR spectra of all samples (Fig. 6), exhibit an absorption band at 3560 cm^{-1} attributed to the
225 stretching $\nu \text{Fe}^{3+}_2\text{-OH}$ vibrations characterizing synthetic as well as natural nontronites (Goodman
226 et al., 1976; Gates, 2005; Gates, 2008; Decarreau et al., 2008; Petit et al., 2015; Baron et al., 2016;
227 Madejová et al., 2017). However, the intensity of this band, when normalized to the main $\nu \text{Si-O}$
228 band (997- 1012 cm^{-1}), increases over synthesis time whereas the FWHM decreases (Table 4).
229 These observations substantiate the increase in crystallinity of the nontronite samples with the
230 synthesis time (Decarreau et al., 2008; 2014). This trend is well correlated with the increase in
231 intensity of the band at 815 cm^{-1} (Fig. 6) attributed to the bending (δ) $\text{Fe}^{3+}_2\text{-OH}$ vibrations
232 (Goodman et al., 1976; Gates, 2005; Gates, 2008; Decarreau et al., 2008; Petit et al., 2015; Baron
233 et al., 2016; Madejová et al., 2017). The $\nu \text{Si-O}$ band is located at 1012 cm^{-1} for the 1 day sample,
234 and shifts down to 997 cm^{-1} for the 62 and 183 days samples (Fig. 6, Table 4). Simultaneously, the
235 intensity of the band at 706 cm^{-1} due to $^{54}\text{Fe}^{3+}\text{-O}$ increases and the $\text{Si}^{4+}\text{-O-}^{56}\text{Fe}^{3+}$ absorption band
236 shifts from 493 cm^{-1} up to 488 cm^{-1} (Decarreau et al., 2008; Petit et al., 2015; Baron et al., 2016).
237 These features indicate an increase in the $^{54}\text{Fe(III)}$ content of the synthetic nontronites (Petit et al.,
238 2015; Baron et al., 2016) which is estimated from the position of the $\nu \text{Si-O}$ band using the equation
239 given by Baron et al. (2016). The $^{54}\text{Fe(III)}$ (x) content evolves from 0.46 (1 day sample) to 0.73
240 (183 days sample) per half-unit formula (Table 4). MIR spectra of samples obtained after 62 and
241 183 days of synthesis are very similar (Fig. 6) revealing the absence of structural evolution between
242 these two samples.

243 The MIR spectrum of the 183 days sample exhibits discrete shoulders at 962 cm^{-1} , 647 cm^{-1} , and
244 565 cm^{-1} due to the occurrence of aegirine (Fig. 6) (Zhang et al., 2002), although aegirine is not
245 identified in the corresponding XRD pattern (Fig. 2).

246 TEM observations of the 1 day, 6 days, 31 days, and 183 days samples reveal nontronite particles,
247 forming foliated aggregates characteristic of smectites (Fig. 7). The 1 day sample exhibits a particle
248 size heterogeneity (the diameter of particles varies from 10 - 50 nm up to > 100 nm) and contains
249 some free lath-shaped nontronite particles of one hundred nm in length (Fig. 7a and 7b). The
250 particle size heterogeneity decreases for the 6 days sample (Figs. 7c and 7d), whereas the nontronite
251 particles overall appear much larger and thicker (Fig. 7d). This trend reflects a growth step of
252 nontronite particles. Lath-shaped nontronite particles are also observed in the 6 days sample (Fig.
253 7d). The 31 days sample is composed of some free nontronite laths of 200 up to 500 nm in length
254 (Fig. 7e) and large aggregates of small rounded particles of around 50 - 100 nm in diameter (Figs.
255 7e and 7f). The 183 days sample is made of foliated aggregates composed of lath shaped nontronite
256 particles having a relatively homogeneous size (100 - 200 nm) (Fig. 7g). This sample is also
257 composed of some smaller rounded particles (20 - 50 nm in diameter). However, few aegirine
258 crystals are observed in the 183 days sample (Fig. 7h). The detection of aegirine is facilitated by a
259 higher disaggregation of this sample. No particle of hematite is identified in all samples of the
260 experiments at $\text{pH}_i = 12$.

261

262 **3.2.3 Nontronite series synthesized at $\text{pH}_i = 13.3$**

263 Powder XRD patterns of samples having the shortest times of hydrothermal treatment (i.e., from 1
264 to 15 days samples) exhibit reflections at 12.19 Å (001), 4.61 Å (02-11), 2.63 Å (13-20), and 1.545
265 - 1.552 Å (06,33) corresponding to Na-nontronites (Fig. 3). No other crystalline phase is evidenced
266 in these samples. The (06, 33) reflection shifts from 1.545 Å to 1.552 Å for the 1 day and 15 days
267 samples, respectively (Fig. 3b), indicating an increase, with time, in the $^{41}\text{Fe(III)}$ content of
268 synthesized nontronites as for the series synthesized at $\text{pH}_i = 12$. The XRD pattern of the 31 days
269 sample reveals nontronite reflections and aegirine ones at 4.42 Å (011), 2.99 Å (121), 2.90 Å (310),
270 2.54 Å (031), 2.47 Å (-321), and 2.20 Å (-312) (Clark et al., 1969; Nolan, 1969; Redhammer et al.,
271 2000; Decarreau et al., 2004). The (06,33) reflection of the 31 days sample appears at the same
272 position than for the 15 days sample indicating a similar $^{41}\text{Fe(III)}$ content for both nontronites. For
273 the longest experiments (i.e., for 62 days and 183 days samples), XRD patterns display aegirine
274 reflections cited above plus the one at 6.37 Å (110) and hematite reflections at 3.67 Å (012) and
275 2.69 Å (104) (Brindley and Brown, 1980).

276 The MIR spectra of the 1, 6 and 15 days samples (Fig. 8) exhibit the absorption bands characteristic
277 of nontronite. The ν Si-O nontronite band shifts from 974 to 962 cm^{-1} for 1 and 15 days samples,
278 respectively (Fig. 8, Table 4). The intensity of the $^{44}\text{Fe}^{3+}$ -O absorption band at 711 cm^{-1} increases
279 in intensity with the synthesis time, while the Si^{4+} -O- $^{56}\text{Fe}^{3+}$ band shifts from 485 cm^{-1} (1 day
280 sample) to 483 cm^{-1} (15 days sample). All these features indicate an increase in the $^{44}\text{Fe(III)}$ content
281 of synthetic nontronites (Petit et al., 2015; Baron et al., 2016). Using the equation given in Baron
282 et al. (2016), the $^{44}\text{Fe(III)}$ amounts are estimated to be 1.16 (1 day sample) and 1.38 (15 days
283 sample) per half-unit formula (Table 4). The MIR spectrum of the 31 days sample exhibits a
284 mixture of bands attributed to aegirine (broad massif of bands between 1100 and 1020 cm^{-1} , and
285 bands at 647, 566, and 450 cm^{-1}), and to nontronite having a high $^{44}\text{Fe(III)}$ content (Table 4; Fig.
286 8). The MIR spectra of the 62 days and 183 days samples exhibit the characteristic features of
287 aegirine at 1071, 1044, 1023, 963, 859, 734, 647, 566, 545, 504, and 450 cm^{-1} (Fig. 8) (Zhang et
288 al., 2002).

289 TEM observations of the 15 days sample show nontronite particles forming foliated aggregates
290 characteristic of smectites, associated with aegirine crystals (Figs. 9a, 9b, and 9c). Nontronite
291 particles exhibit a higher blocky-like shape than those having a lath shape previously observed for
292 the series synthesized at $\text{pH}_i = 12$. Two populations of particles are observed, the first one being
293 hundreds of nm in diameter (Fig. 9a: B) and the second one being composed of particles up to 50
294 nm in diameter (Fig. 9a: A). This latter population is largely composed of rounded nontronite
295 particles (Fig. 9b). For the 31 days sample, TEM observations reveal nontronites aggregates
296 composed of large particles of around 500 nm in diameter or rounded particles of 50 - 100 nm in
297 diameter (Figs. 9d, 9e, and 9f). Aegirine crystals of few μm in length with a prismatic shape are
298 also identified in association with hematite (Figs. 9e and 9f). As mentioned before, the rounded
299 shape of nontronites particles is evidence of their partial dissolution in favor of aegirine and
300 hematite. Finally, aegirine and hematite are the only minerals observed for the 183 days sample
301 (Figs. 9g and 9h).

302

303 3.3 Thermodynamics

304 To assess the reaction pathway from nontronite to aegirine and hematite, stability fields of
305 nontronite with different $^{44}\text{Fe(III)}$ content ($x = 0.5, 0.75, 1.15$ and 1.35), aegirine, hematite, and

306 ferripyrophyllite were calculated at 150 °C (Fig. 10). Note that, the calculated stability field of
307 nontronite tends to enlarge with the increase in $^{44}\text{Fe(III)}$ content (Fig. 10).

308 The chemical properties of solutions at the end of synthesis (Table 2) were plotted for the series at
309 $\text{pH}_i = 12$ in Fig. 10a and for the series at $\text{pH}_i = 13.3$ in Fig. 10b. For all syntheses realized at $\text{pH}_i =$
310 12, solutions are far from the stability field of nontronite, but close to the aegirine-hematite tie-line
311 (Fig. 10a). For the series at $\text{pH}_i = 13.3$, the 1 day solution is close to the triple point aegirine-
312 hematite-nontronite ($x = 1.15$) (Fig. 10b); most of the other solutions fall near the theoretical
313 aegirine-nontronite ($x = 1.35$) tie-line while the 62 days solution is shifted toward the stability field
314 of hematite (Fig. 10b). The chemistry of the experimental system, that is not stoichiometric with
315 respect to aegirine ($\text{Fe/Si} = 0.73$ in the gel precursor instead of 0.5 for aegirine), induces the
316 crystallization of hematite.

317

318 **4 Discussion**

319 **4.1 Na-Nontronite metastability**

320 MIR, XRD, and TEM data, whatever the value of pH_i , evidence a massive dissolution of the gel
321 precursor in favor of the crystallization of nontronite after only 1 day of hydrothermal treatment
322 (Fig. 11). TEM observations do not exhibit the characteristic features of amorphous solid materials
323 (Fig. 5) in the synthetic nontronite samples (Fig. 7 and 9). TEM images reveal large aggregates of
324 nontronite particles, which may contain some residues of the precursor. No clear hump in the
325 overall XRD intensity above the baseline around 30° (2θ) is observed, which suggests very low
326 amounts of remaining amorphous material in 1 day synthetic products (Fig. 2 and 3). The MIR data
327 also argue for a massive dissolution of the starting gel in favor of the nontronite crystallization that
328 is clearly evidenced by the shift of the ν Si-O band (Fig. 4). This fast reaction is probably facilitated
329 by the presence of already organized TOT-like structures (i.e., building blocks) in the gel precursor
330 as previously mentioned by Decarreau et al. (2008).

331 From a series of nontronites synthesized at pH from 10 up to 14 for 6 days, Baron et al. (2016)
332 demonstrated that the increase in $^{44}\text{Fe(III)}$ content of the nontronites is linked to the increase of
333 pH_f values (Fig. 12). In the present study, the $^{44}\text{Fe(III)}$ contents of the synthesized nontronites
334 increase for both series of pH, that are in agreement with the slight increase in pH_f , (Fig. 12; Table
335 1). However, the two reactions: low $^{44}\text{Fe(III)}$ -nontronite > high $^{44}\text{Fe(III)}$ -nontronite; and nontronite
336 > aegirine would induce a decrease in pH. Thus, the slight increase in pH_f is likely due to the

337 dissolution of a small amount of residual gel, trapped in smectite aggregates, in favor of the
338 nontronite crystallization because this reaction induces an increase in pH (Decarreau, 1985). The
339 short amount of time required to synthesize these clay minerals allows the crystal chemistry of the
340 synthesized nontronites to evolve over time.

341 For the series at $\text{pH}_i = 12$, the principal phenomenon observed between 1 and 62 days is the increase
342 in the nontronite particle size (crystal growth) and the increase in crystallinity (crystal defects
343 resorption). The coexistence of large laths with small rounded particles (Figs. 7e and 7f) may result
344 from the “Ostwald’s ripening” process (Ostwald, 1897); i.e., the small particles dissolve in favor
345 of the growth of larger ones. After 62 days of hydrothermal treatment, the reaction nontronite >
346 aegirine is observed (Fig. 11; Table 1).

347 For the series at $\text{pH}_i = 13.3$, nontronite is the single mineral identified into the solid phase until 15
348 days. For longer ageing times, nontronite particles rapidly dissolve in favor of the crystallization
349 of aegirine and hematite, until the complete dissolution of nontronite between 31 and 62 days (Fig.
350 11; Table 1). The possible occurrence of few aegirine crystals into the 1 and 15 days samples
351 remains, however, an open question.

352 These results on both series reveal that all the synthesized nontronites, whatever their amounts of
353 $^{44}\text{Fe(III)}$, appear as metastable phases at 150 °C in this Na-Fe(III)-Si-O-OH system; the stable
354 paragenesis being aegirine and hematite in these experiments. The rate of the reaction nontronite >
355 aegirine + hematite is, however, strongly influenced by the pH of the solution (Fig. 11; Table 1).
356 Similarly, Nagase et al. (1999) synthesized in 1 day at 100 and 200 °C aegirine at pH_f near 13 and
357 nontronite at pH_f near 12. Due to the link between pH_f and the crystal chemistry of nontronites
358 (Baron et al., 2016), nontronites with high levels of $^{44}\text{Fe(III)}$ appear as more labile metastable
359 phases than nontronites with low $^{44}\text{Fe(III)}$ amounts in the given conditions of the present study.
360 The increase in temperature also favors the formation of aegirine. For similar pH_i near 12,
361 Decarreau et al. (2008, 2004) synthesized nontronites having a $^{44}\text{Fe(III)}$ content of 0.75 at
362 temperatures from 75 to 150 °C, and aegirine + ϵ nontronite at 200 °C. Similarly, Kopp and Harris
363 (1967) obtained aegirine at 425 °C and nontronite at 365 °C during the synthesis of grunerite
364 (Fe(II)-amphibole).

365 This suite of experiments indicates that nontronite is more labile than aegirine in these
366 hydrothermal conditions. However, Eggleton (1975) observed the formation of nontronite at the
367 expense of hedenbergite (Ca-clinopyroxene) in the conditions of Earth’s surface. These

368 observations show that nanoparticles of nontronite are more stable than pyroxene in weathering
369 conditions. The mineralogical reaction involving nontronite and pyroxene could thus be reversible.

370 **4.2 Thermodynamics: possible explanation of nontronite metastability**

371 In the present study, nontronites form at 150 °C at the early stage of the experiments, although the
372 chemical compositions of solutions are far from the nontronite stability field (Fig. 10). This
373 observation is consistent with the status of nontronite as labile metastable phase, kinetically favored
374 with respect to aegirine, which appears to be the stable silicate, given the conditions of the present
375 study. This reaction pathway looks like it obeys to the Ostwald's step rule (Ostwald, 1897). These
376 results are in agreement with the conclusion of Lippmann (1982, 1979, 1977) and Eberl (1978)
377 indicating that clay minerals can be formed for kinetics reasons far from the thermodynamic
378 equilibrium.

379 The chemical compositions of solutions during synthesis are located near the tie-line aegirine-
380 hematite or inside the stability field of aegirine (Fig. 10). These data suggest that the chemistry of
381 the solutions is constrained rather by the precipitation of aegirine and that very small amounts of
382 aegirine may form in the early stage of syntheses.

383 The thermodynamic stability field of nontronite is, however, calculated using “standard” data that
384 do not take into account the effect of particle size. Indeed, it is now well known that the decrease
385 in particle size of a mineral induced modification of its stability field due to change of the surface
386 energy, as observed for alumina (McHale et al., 1997), hydroxyapatite (Tang et al., 2004), TiO₂
387 (Zhang and Banfield, 1998), and Al- or Fe(III)-[oxi(hydr)]oxide minerals (Trolard and Tardy,
388 1987; Hochella et al., 2008; Navrotsky et al., 2008). For Fe(III)-[oxi(hydr)]oxides, Navrotsky et al.
389 (2008) concluded: “The competition between surface enthalpy and the energetics of phase
390 transformation leads to the general conclusion that polymorphs metastable as micrometer-sized or
391 larger crystals can often be thermodynamically stabilized at the nanoscale”. Consequently,
392 minerals having high hydration and high surface area can often be formed and thermodynamically
393 stabilized at small particle sizes (Hochella et al., 2008; Navrotsky et al., 2008). Moreover, hydrous
394 minerals can persist and their stability field can significantly expand to higher temperatures if the
395 growth rates of the metastable phase are slower than the phase reaction rate (Hochella et al., 2008;
396 Navrotsky et al., 2008). However, these two studies involved isochemical phase reaction between
397 two polymorphs, which is not the case in our study. Indeed, the reaction observed in our
398 experiments involved for the first time a phyllosilicate (nontronite), an inosilicate (aegirine) and an

399 oxide (hematite). All assumptions on the isochemical phase reactions are supported by
400 measurements of minerals thermodynamic properties at the nanoscale. However, these data are
401 lacking for nontronite and aegirine + hematite. Nevertheless, we suggest during synthesis
402 experiments, that nontronite probably forms first due to specific thermodynamic properties (surface
403 energy) linked to their very small particles size (nanoparticles) and high hydration properties. At
404 the first stage of synthesis experiments, nanoparticles of nontronite are thermodynamically more
405 competitive to form, but dissolve, when they reach a critical size (100 - 200 nm), in favor of the
406 precipitation of the stable mineral assemblage aegirine + hematite. It is interesting to note that, in
407 experiments at $\text{pH}_i = 12$, the diameter of nontronite particles did not increase markedly (from 50-
408 100 nm up to 200 nm) after six months while the first detected crystals of aegirine in the 183 days
409 sample are already about 500 nm long (Fig. 7h). Nontronite persists only as metastable
410 nanoparticles while stable aegirine crystals enlarge up to more than 3 μm during the same time at
411 $\text{pH}_i = 13.3$ (Fig. 9d).

412

413 **4.3 Time vs. temperature during nontronite synthesis**

414 In this study, an increase in time of experiments induces an increase in crystallinity (resorption of
415 defects) of synthesized nontronites (see section 3.2.2 and 3.2.3). An equivalent effect of an increase
416 in temperature is observed during similar syntheses of nontronites between 75 and 100 °C
417 (Decarreau et al., 2008), but the increase in temperature up to 150 °C did not induce an increase in
418 crystallinity. These authors concluded that it was not possible to increase the crystallinity of
419 nontronites by increasing the time or the temperature of synthesis. In fact, the metastable nontronite
420 crystals synthesized by Decarreau et al. (2008) had probably reached their critical size before
421 beginning to dissolve in favor of the aegirine crystallization. Klopogge et al. (1999) noted that
422 most of the smectite syntheses do not have sufficient ageing time to ascertain that the synthetic
423 products are the thermodynamically stable phases. These authors also stated that many synthetic
424 products may be metastable, inducing the formation of kinetically favorable phases.

425 The nontronites synthesized by Decarreau et al. (2008) have been studied for the crystal growth of
426 clay particles, using low-pressure argon adsorption (Decarreau et al. 2014), assuming that time and
427 temperature play equivalent roles. In light of the results of the present study, the role of synthesis
428 time (ageing time) is not necessarily analogous to the one of the temperature during the clay
429 minerals formation in batch experiments.

430

431 **5 Geological Implications**

432 **5.1 Metalliferous sediments, Atlantis II deep, Red Sea**

433 The metalliferous sediments of the Atlantis II deep, Red Sea have been intensively studied since
434 their discovery in 1965 (see an exhaustive review in Laurila et al., 2015). They consist of about 20
435 m of fine-grained, laminated sediments, composed of oxides, sulfides, silicates, and carbonates,
436 deposited from – 25,000 BP (Anschutz and Blanc, 1995a). These sediments contain detrital and
437 authigenic clays, Fe-nontronites being the most common authigenic ones (Anschutz and Blanc,
438 1995a; Laurila et al., 2015). Fe-nontronites occur notably in the upper part of sediments (Badaut et
439 al., 1990; Anschutz and Blanc, 1995a). They formed during diagenesis from initial amorphous Si-
440 Fe-O, OH precipitates (Anschutz and Blanc, 1995a; Laurila et al., 2015).

441 A core (n°684) was collected in 1985 in the western basin of Atlantis II deep during the
442 “Hydrotherm” cruise of the RV Marion Dufresne (Blanc et al., 1986). The porosity of the core
443 remains above 90% in its upper part. Badaut et al. (1992) described, in the core 684, an authigenic
444 Fe-rich nontronite at a depth of 2.6 m ($^{[4]}[\text{Si}_{13.62}\text{Al}_{0.08}\text{Fe(III)}_{0.3}]^{[6]}[\text{Fe(III)}_{1.84}\text{Mg}_{0.13}\text{Al}_{0.03}]\text{O}_{10}(\text{OH})_2$
445 $[\text{K}_{0.12}\text{Na}_{0.17}(\text{Mg}, \text{Ca})_{0.11}]$). From oxygen isotopes data, the formation temperature of this nontronite
446 is 70 °C (Decarreau et al., 1990). The chemistry of the pore water of sediments in which the
447 nontronite formed is available (Si \approx 100 $\mu\text{mol L}^{-1}$, Na = 5000 $\mu\text{mol L}^{-1}$, Mg = 30 $\mu\text{mol L}^{-1}$, K = 60
448 $\mu\text{mol L}^{-1}$, Ca = 130 $\mu\text{mol L}^{-1}$, and pH = 8.24) (Blanc et al., 1986; Anschutz and Blanc, 1995b;
449 Anschutz et al., 2000). Activities and speciation of elements in solution were calculated as above
450 for Fig. 10.

451 The dissolved Na in Atlantis II deep sediments pore water being high, there is a great analogy
452 between authigenic nontronite in the Red Sea and the nontronite syntheses described here. As
453 predicted by Baron et al. (2016), the authigenic nontronite formed at pH = 8.24 would exhibit a
454 low Fe(III) for Si tetrahedral substitution. The chemistry of the pore water was reported on a
455 thermodynamic diagram similar to those used for synthetic nontronites, calculated at 70 °C for a
456 $^{[4]}[\text{Si}_{3.7}\text{Fe(III)}_{0.3}]^{[6]}\text{Fe(III)}_2\text{O}_{10}(\text{OH})_2\text{Na}_{0.3}$ nontronite similar to the nontronite of core 684 (Fig.13).
457 The plot of pore water is located far away from the stability field of nontronite and near the
458 aegirine-hematite (or goethite) equilibrium line, as previously observed for synthetic nontronites
459 (Fig. 10). The Fe-nontronites from the Atlantis II deep are then formed as metastable clay minerals
460 kinetically favored, persisting during more than 10,000 years without any observation of aegirine.

461 However, the metastable nontronite formed in the Atlantis II deep at a lower temperature than the
462 one used for the synthesis experiments presented here (70 °C instead of 150 °C) and at lower pH
463 (8.24 instead of 12 or 13.3), these two parameters having a strong influence on the kinetic of
464 nontronite > aegirine + hematite reaction (see above). Despite the predominance of Na vs. K, Mg,
465 and Ca in pore water, the exchangeable cations of the nontronite from core 684 are K, Na, and (Mg,
466 Ca) in quite equal amounts. Coupled with the occurrence of octahedral Mg, the nature of these
467 cations may also prevent the dissolution of nontronite in favor of the aegirine crystallization.

468

469 **5.2 Post-magmatic Fe-clays**

470 Oyawoye & Hirst (1964) observed Fe(III)-rich smectites associated with primary euhedral quartz,
471 feldspars, and biotites in fresh granite. No dissolution features having been observed on the surface
472 of the primary minerals, authors concluded that the Fe(III)-rich smectites had a primary origin.
473 Similarly, Meunier et al. (2008) described nontronite (among other clay minerals) associated with
474 apatites and euhedral pyroxenes in diktytaxitic voids of submarine lava flows. Dissolution features
475 also lacked in these minerals. Because clay minerals were enriched in Rare Earth and incompatible
476 elements, the authors suggested a post-magmatic stage origin of clay minerals at temperatures
477 between 70 and 100 °C. Berger et al. (2014) observed, in other lavas flows, the occurrence of
478 Fe(III)-rich clay minerals having a post-magmatic origin during lava outgassing between 100 and
479 300 °C. Meunier et al. (2008) and Berger et al. (2014) concluded that anhydrous mafic minerals
480 (pyroxenes) and Fe(III)-clay minerals could be simultaneously formed during these processes,
481 despite the fact that syn-crystallization of hydrated phases with mafic minerals is unusual. In the
482 light of this present study, the syn-formation of pyroxene and Fe(III)-rich clay minerals is possible
483 at a temperature as low as 150 °C. Moreover, the reaction pathway observed suggests that Fe-clays
484 formed first, kinetically favored, and are replaced later by pyroxene.

485

486 **5.3 Metastability of smectites**

487 Despite the study of the Na-nontronite in the Na-Fe(III)-Si-O-OH at 150 °C, which is not
488 representative of the whole of smectites, some important insights can be obtained from the present
489 experimental study, notably on the role of substitutions on their size and stability. Morse and Casey
490 (1988) and May et al. (1986) proposed that the high chemical heterogeneity of smectites induced
491 their metastability. The present study shows that even in a very simple chemical system, such as

492 Na-Fe(III)-Si-O-OH, smectite (here nontronite) can be metastable even at a temperature common
493 for smectite formation (i.e., 150 °C). Therefore, the chemical heterogeneity of smectites is not the
494 only parameter responsible for their metastability.

495 Similarly, Meunier (2006) suggested that the large amounts of crystal defects of clay minerals,
496 notably due to cations substitutions, explained their small particle size. The present study showed
497 that in the case of a smectite with a very simple chemistry (Na-Fe(III)-Si-O-OH), and without any
498 octahedral substitution, the small size of smectite particles is due to their metastability and rather
499 reflects the particle size limit beyond which smectite is dissolved to form the stable mineral
500 assemblage, aegirine + hematite in the context of the present study.

501

502 **6 Conclusions**

503 For the first time, the metastability of Na-nontronite is evidenced experimentally in the conditions
504 used for this study. Another main point is the mineralogical reaction occurring through an
505 Ostwald's step rule between a metastable phyllosilicate (nontronite) and a stable inosilicate
506 (pyroxene). It is more likely that the crystallization of the Na-nontronite as metastable phase is
507 linked to its nanoscale particle size. Consequently, the use of thermodynamic equilibrium models
508 to predict the formation and evolution of Na-nontronite can be questioned if these models fail to
509 take into account the size dependence of the thermodynamic properties and their effects on the
510 kinetics of reactions (nucleation, growth, phase transition...).

511 It remains an open question as to whether the results found for Na-nontronite could be generalized
512 to all smectites. Answering this question would require further experimental studies, and most
513 importantly long-time experiments.

514

515 **Acknowledgments**

516 P. Vieillard and J. Rousseau (IC2MP) are acknowledged for their useful help concerning
517 respectively the calculation of thermodynamic properties of nontronites and the TEM analyses.
518 The European Union (ERDF), "Région Nouvelle Aquitaine", and French « Ministère de
519 l'Enseignement Supérieur et de la Recherche » are also acknowledged for their financial supports.

520

521 **References**

- 522 Aja S. U. and Rosenberg P. E. (1996) The thermodynamic status of compositionally-complex
523 clay minerals; discussion of Clay mineral thermometry; a critical perspective. *Clays Clay*
524 *Miner.* **44**, 560–568.
- 525 Aja S. U. and Rosenberg P. E. (1992) The thermodynamic status of compositionally-variable clay
526 minerals; a discussion. *Clays Clay Miner.* **40**, 292–299.
- 527 Anschutz P. and Blanc G. (1995a) Chemical mass balances in metalliferous deposits from the
528 Atlantis II Deep, Red Sea. *Geochim. Cosmochim. Acta* **59**, 4205–4218.
- 529 Anschutz P. and Blanc G. (1995b) Geochemical dynamics of the Atlantis II Deep (Red Sea):
530 silica behavior. *Mar. Geol.* **128**, 25–36.
- 531 Anschutz P., Blanc G., Monnin C. and Boulègue J. (2000) Geochemical dynamics of the Atlantis
532 II Deep (Red Sea): II. Composition of metalliferous sediment pore waters. *Geochim.*
533 *Cosmochim. Acta* **64**, 3995–4006.
- 534 Badaut D., Blanc G. and Decarreau A. (1990) Variation des minéraux argileux ferrifères, en
535 fonction du temps et de l'espace, dans les dépôts métallifères de la fosse Atlantis II en
536 Mer Rouge. *Comptes Rendus Académie Sci. Sér. 2 Mécanique Phys. Chim. Sci. Univers*
537 *Sci. Terre* **310**, 1069–1075.
- 538 Badaut D., Decarreau A. and Besson G. (1992) Ferripyrophyllite and related Fe³⁺-rich 2:1 clays
539 in Recent deposits of Atlantis II Deep, Red Sea. *Clay Miner.* **27**, 227–244.
- 540 Baron F., Petit S., Tertre E. and Decarreau A. (2016) Influence of aqueous Si and Fe speciation
541 on tetrahedral Fe(III) substitutions in nontronites: a clay synthesis approach. *Clays Clay*
542 *Miner.* **64**, 230.
- 543 Berger G., Meunier A. and Beaufort D. (2014) Clay mineral formation on Mars: Chemical
544 constraints and possible contribution of basalt out-gassing. *Planet. Space Sci.* **95**, 25–32.
- 545 Blanc G., Boulègue J., Badaut D. and Stouff P. (1986) Premiers résultats de la campagne
546 océanographique Hydrocherm (mai 1985) du Marion-Dufresne sur la fosse Aûancis II
547 (Mer Rouge). *Comptes Rendus Académie Sci. - Ser. IIA - Earth Planet. Sci.* **302**, 175–180.
- 548 Blanc P., Vieillard P., Gailhanou H., Gaboreau S., Gaucher É., Fialips C. I., Madé B. and Giffaut
549 E. (2015) A generalized model for predicting the thermodynamic properties of clay
550 minerals. *Am. J. Sci.* **315**, 734–780.
- 551 Brigatti M. F. (1983) Relationships between composition and structure in Fe-rich smectites. *Clay*
552 *Miner.* **18**, 177–186.

553 Brindley G. W. and Brown G. (1980) *Crystal structures of clay minerals and their X-ray*
554 *identification*. Monograph no. 5., Mineralogical Society, London.

555 Carter J., Loizeau D., Mangold N., Poulet F. and Bibring J.-P. (2015) Widespread surface
556 weathering on early Mars: A case for a warmer and wetter climate. *Icarus* **248**, 373–382.

557 Carter J., Poulet F., Bibring J.-P., Mangold N. and Murchie S. (2013) Hydrous minerals on Mars
558 as seen by the CRISM and OMEGA imaging spectrometers: Updated global view. *J.*
559 *Geophys. Res. Planets* **118**, 831–858.

560 Clark J. R., Appleman D. E. and Papike J. J. (1969) Crystal-chemical characterization of
561 clinopyroxenes based on eight new structure refinements. *Mineral. Soc. Am. - Spec. Pap.*
562 **2**, 31–50.

563 Decarreau A. (1985) Partitioning of divalent transition elements between octahedral sheets of
564 trioctahedral smectites and water. *Geochim. Cosmochim. Acta* **49**, 1537–1544.

565 Decarreau A., Badaut D. and Blanc G. (1990) Origin and temperature formation of Fe-rich clays
566 from Atlantis II deep deposits (Red Sea). An oxygen isotopic geochemistry approach.
567 *Chem. Geol.* **84**, 363–364.

568 Decarreau A., Petit S., Andrieux P., Villieras F., Pelletier M. and Razafitianamaharavo A. (2014)
569 Study of low-pressure argon adsorption on synthetic nontronite: Implications for smectite
570 crystal growth. *Clays Clay Miner.* **62**, 102–111.

571 Decarreau A., Petit S., Martin F., Farges F., Vieillard P. and Joussein E. (2008) Hydrothermal
572 synthesis, between 75 and 150 °C, of high-charge, ferric nontronites. *Clays Clay Miner.*
573 **56**, 322–337.

574 Decarreau A., Petit S., Vieillard P. and Dabert N. (2004) Hydrothermal synthesis of aegirine at
575 200 °C. *Eur. J. Mineral.* **16**, 85–90.

576 Eberl D. (1978) Reaction series for dioctahedral smectites. *Clays Clay Miner.* **26**, 327–340.

577 Eggleton R. A. (1977) Nontronite; chemistry and X-ray diffraction. *Clay Miner.* **12**, 181–194.

578 Eggleton R. A. (1975) Nontronite topotaxial after hedenbergite. *Am. Mineral.* **60**, 1063–1068.

579 Essene E. J. and Peacor D. R. (1995) Clay mineral thermometry; a critical perspective. *Clays*
580 *Clay Miner.* **43**, 540–553.

581 Essene E. J. and Peacor D. R. (1997) Illite and smectite; metastable, stable or unstable? Further
582 discussion and a correction; reply. *Clays Clay Miner.* **45**, 116–122.

583 Gates W. P. (2008) Cation mass-valence sum (CM-VS) approach to assigning OH-bending bands
584 in dioctahedral smectites. *Clays Clay Miner.* **56**, 10–22.

585 Gates W. P. (2005) The Application of Vibrational Spectroscopy to Clay Minerals and Layered
586 Double Hydroxides. In *Infrared spectroscopy and the chemistry of dioctahedral smectites*
587 (ed. J. Theo Kloprogge). The Clay Minerals Society, Aurora, CO. pp. 125–168.

588 Goodman B. A., Russell J. D., Fraser A. R. and Woodhams F. W. D. (1976) A Mössbauer and
589 I.R. spectroscopic study of the structure of nontronite. *Clays Clay Miner.* **24**, 53–59.

590 Gunnarsson I. and Arnórsson S. (2000) Amorphous silica solubility and the thermodynamic
591 properties of H_4SiO_4 in the range of 0 to 350 °C at P_{sat} . *Geochim. Cosmochim. Acta* **64**,
592 2295–2307.

593 Hemingway B. S. (1990) Thermodynamic properties for bunsenite, NiO, magnetite, Fe_3O_4 , and
594 hematite, Fe_2O_3 , with comments on selected oxygen buffer reactions. *Am. Mineral.* **75**,
595 781–790.

596 Heuser M., Andrieux P., Petit S. and Stanjek H. (2013) Iron-bearing smectites: a revised
597 relationship between structural Fe, b cell edge lengths and refractive indices. *Clay Miner.*
598 **48**, 97–103.

599 Hochella M. F., Lower S. K., Maurice P. A., Penn R. L., Sahai N., Sparks D. L. and Twining B.
600 S. (2008) Nanominerals, Mineral Nanoparticles, and Earth Systems. *Science* **319**, 1631–
601 1635.

602 Kittrick J. A. (1971a) Montmorillonite Equilibria and the Weathering Environment. *Soil Sci. Soc.*
603 *Am. J.* **35**, 815–820.

604 Kittrick J. A. (1971b) Stability of Montmorillonites: I. Belle Fourche and Clay Spur
605 Montmorillonites. *Soil Sci. Soc. Am. J.* **35**, 140–145.

606 Kittrick J. A. (1971c) Stability of Montmorillonites: II. Aberdeen Montmorillonite. *Soil Sci. Soc.*
607 *Am. J.* **35**, 820–823.

608 Kittrick J. A. and Peryea F. J. (1988) Experimental Validation of the Monophase Structure Model
609 for Montmorillonite Solubility. *Soil Sci. Soc. Am. J.* **52**, 1199–1201.

610 Kittrick J. A. and Peryea F. J. (1989) The Monophase Model for Magnesium-Saturated
611 Montmorillonite. *Soil Sci. Soc. Am. J.* **53**, 292–295.

612 Kloprogge J. T., Komarneni S. and Amonette J. E. (1999) Synthesis of smectite clay minerals; a
613 critical review. *Clays Clay Miner.* **47**, 529–554.

614 Kopp O. C. and Harris L. A. (1967) Synthesis of Grunerite and Other Phases in the System SiO₂-
615 NaOH-Fe-HaO. *Am. Mineral.* **52**, 1681–1688.

616 Köster H. M., Ehrlicher U., Gilg H. A., Jordan R., Murad E. and Onnich K. (1999) Mineralogical
617 and chemical characteristics of five nontronites and Fe-rich smectites. *Clay Miner.* **34**,
618 579–599.

619 Laurila T. E., Hannington M. D., Leybourne M., Petersen S., Devey C. W. and Garbe-Schönberg
620 D. (2015) New insights into the mineralogy of the Atlantis II Deep metalliferous
621 sediments, Red Sea. *Geochem. Geophys. Geosystems* **16**, 4449–4478.

622 Lippmann F. (1979) Stability diagrams involving clay minerals. In *Eighth Conference on Clay*
623 *Mineralogy and Petrology in Teplice* Pragues. pp. 153–171.

624 Lippmann F. (1977) The solubility products of complex minerals, mixed crystals, and three-layer
625 clay minerals. *Neues Jahrb. Für Mineral. - Abh.* **130**, 243–263.

626 Lippmann F. (1982) The thermodynamic status of clay minerals. In *Proceedings of the 7th*
627 *International Clay Conference, 1981* Developments in sedimentology. Elsevier,
628 Amsterdam. pp. 475–485.

629 Madejová J., Gates W. P. and Petit S. (2017) IR Spectra of Clay Minerals. In *Developments in*
630 *Clay Science* (eds. W. P. Gates, J. T. Kloprogge, J. Madejová, and F. Bergaya). Infrared
631 and Raman Spectroscopies of Clay Minerals. Elsevier. pp. 107–149.

632 May H. M., Klunnburgh D. G., Helmke P. A. and Jackson M. L. (1986) Aqueous dissolution,
633 solubilities and thermodynamic stabilities of common aluminosilicate clay minerals:
634 Kaolinite and smectites. *Geochim. Cosmochim. Acta* **50**, 1667–1677.

635 McHale J. M., Auroux A., Perrotta A. J. and Navrotsky A. (1997) Surface Energies and
636 Thermodynamic Phase Stability in Nanocrystalline Aluminas. *Science* **277**, 788–791.

637 Meunier A. (2006) Why are clay minerals small? *Clay Miner.* **41**, 551–566.

638 Meunier A., Mas A., Beaufort D., Patrier P. and Dudoignon P. (2008) Clay minerals in basalt-
639 hawaiiite rocks from Mururoa Atoll (French Polynesia). II. Petrography and
640 Geochemistry. *Clays Clay Miner.* **56**, 730–750.

641 Meunier A., Petit S., Ehlmann B. L., Dudoignon P., Westall F., Mas A., El Albani A. and Ferrage
642 E. (2012) Magmatic precipitation as a possible origin of Noachian clays on Mars. *Nat.*
643 *Geosci.* **5**, 739–743.

644 Michalski J. R., Cuadros J., Bishop J. L., Darby Dyar M., Dekov V. and Fiore S. (2015)
645 Constraints on the crystal-chemistry of Fe/Mg-rich smectitic clays on Mars and links to
646 global alteration trends. *Earth Planet. Sci. Lett.* **427**, 215–225.

647 Morse J. W. and Casey W. H. (1988) Ostwald processes and mineral paragenesis in sediments.
648 *Am. J. Sci.* **288**, 537–560.

649 Mustard J. F., Murchie S. L., Pelkey S. M., Ehlmann B. L., Milliken R. E., Grant J. A., Bibring
650 J.-P., Poulet F., Bishop J., Dobreá E. N., Roach L., Seelos F., Arvidson R. E., Wiseman
651 S., Green R., Hash C., Humm D., Malaret E., McGovern J. A., Seelos K., Clancy T.,
652 Clark R., Marais D. D., Izenberg N., Knudson A., Langevin Y., Martin T., McGuire P.,
653 Morris R., Robinson M., Roush T., Smith M., Swayze G., Taylor H., Titus T. and Wolff
654 M. (2008) Hydrated silicate minerals on Mars observed by the Mars Reconnaissance
655 Orbiter CRISM instrument. *Nature* **454**, 305–309.

656 Nagase T., Iwasaki T., Ebina T., Hayashi H., Onodera Y. and Dutta N. C. (1999) Hydrothermal
657 synthesis of Fe-montmorillonite in Si-Fe-Mg system. *Chem. Lett.* **28**, 303–304.

658 Navrotsky A., Mazeina L. and Majzlan J. (2008) Size-Driven Structural and Thermodynamic
659 Complexity in Iron Oxides. *Science* **319**, 1635–1638.

660 Neumann, A., Petit, S., & Hofstetter, T.B. (2011) Evaluation of redox-active iron sites in
661 smectites using middle and near infrared spectroscopy. *Geochimica et Cosmochimica*
662 *Acta*, **75**, 2336–2355.

663 Nolan J. (1969) Physical properties of synthetic and natural pyroxenes in the system diopside-
664 hedenbergite-acmite. *Mineral. Mag.* **37**, 216–229.

665 Nývlt J. (1995) The Ostwald Rule of Stages. *Cryst. Res. Technol.* **30**, 443–449.

666 Ostwald W. (1897) Studien über die Bildung und Umwandlung fester Körper. 1. Abhandlung:
667 Übersättigung und Überkaltung. *Z. Für Phys. Chem.* **22**, 289–330.

668 Oyawoye M. O. and Hirst D. M. (1964) Occurrence of a montmorillonite mineral in the Nigerian
669 younger granites at Ropp, Plateau Province, Northern Nigeria. *Clay Miner.* **5**, 427–433.

670 Parkhurst D. L. and Appelo C. A. J. (2013) Description of input and examples for PHREEQC
671 version 3 — A computer program for speciation, batch-reaction, one-dimensional
672 transport, and inverse geochemical calculations. *US Geol. Surv. Tech. Methods*.

673 Petit S., Baron F. and Decarreau A. (2017) Synthesis of nontronite and other Fe-rich smectites: a
674 critical review. *Clay Miner.* **52**, 469–483.

675 Petit S., Decarreau A., Gates W., Andrieux P. and Grauby O. (2015) Hydrothermal synthesis of
676 dioctahedral smectites: The Al–Fe³⁺ chemical series. Part II: Crystal-chemistry. *Appl.*
677 *Clay Sci.* **104**, 96–105.

678 Poulet F., Bibring J.-P., Mustard J. F., Gendrin A., Mangold N., Langevin Y., Arvidson R. E.,
679 Gondet B. and Gomez C. (2005) Phyllosilicates on Mars and implications for early
680 martian climate. *Nature* **438**, 623–627.

681 Redhammer G. J., Amthauer G., Lottermoser W. and Treutmann W. (2000) Synthesis and
682 structural properties of clinopyroxenes of the hedenbergite CaFe²⁺Si₂O₆ - aegirine
683 NaFe³⁺Si₂O₆ solid-solution series. *Eur. J. Mineral.* **12**, 105–120.

684 Robie R. A. and Hemingway B. S. (1995) *Thermodynamic properties of minerals and related*
685 *substances at 298.15 K and 1 bar (10⁵ pascals) pressure and at higher temperatures.*
686 USGS Bulletin 2131, 461 p.

687 Strickland J. D. H. and Parsons T. R. (1972) *A practical handbook of seawater analysis*, Fisheries
688 Research Board of Canada, Ottawa.

689 Stucki, J.W., Goodman, B.A., & Schwertmann, U. (Eds.) (1988) *Iron in Soils and Clay Minerals*,
690 Dordrecht, Holland.

691 Stucki, J.W. (2013) Properties and behaviour of iron in clay minerals. Pp. 559–612 in: *Handbook*
692 *of Clay Science* (Bergaya, F. and Lagaly, G. editors). Elsevier, Amsterdam.

693 Tang R., Wang L. and Nancollas G. H. (2004) Size-effects in the dissolution of hydroxyapatite:
694 an understanding of biological demineralization. *J. Mater. Chem.* **14**, 2341–2346.

695 Thompson J. B. (1955) The thermodynamic basis for the mineral facies concept. *Am. J. Sci.* **53**,
696 65–103.

697 Trolard F. and Tardy Y. (1987) The stabilities of gibbsite, boehmite, aluminous goethites and
698 aluminous hematites in bauxites, ferricretes and laterites as a function of water activity,
699 temperature and particle size. *Geochim. Cosmochim. Acta* **51**, 945–957.

700 Van Santen R. A. (1984) The Ostwald step rule. *J. Phys. Chem.* **88**, 5768–5769.

701 Wilson M. J. (2013) *Sheet Silicates: Clay Minerals*. The Geological Society. eds. Deer, Howie,
702 and J. Zussman, The Geological Society, London.

703 Zhang H. and Banfield J. F. (1998) Thermodynamic analysis of phase stability of nanocrystalline
704 titania. *J. Mater. Chem.* **8**, 2073–2076.

705 Zhang M., Redhammer J. G., Salje H. E. K. and Mookherjee M. (2002) $\text{LiFeSi}_2\text{O}_6$ and
706 $\text{NaFeSi}_2\text{O}_6$ at low temperatures: an infrared spectroscopic study. *Phys. Chem. Miner.* **29**,
707 609–616.

708

709 **Figure captions:**

710 Figure 1: Structure of the Na-nontronite.

711

712 Figure 2: XRD powder patterns (a) of the series of samples synthesized at $\text{pH}_i = 12$. (b): zoom of
713 the (06,33) reflection.

714

715 Figure 31: XRD powder patterns (a) of the series of samples synthesized at $\text{pH}_i = 13.3$. (b): zoom
716 of the (06,33) reflection.

717

718 Figure 4: MIR spectra of the gel precursor and of a synthesized nontronite (NT10).

719 Figure 5: TEM images of the starting gel.

720

721 Figure 6: MIR spectra of the series of samples synthesized at $\text{pH}_i = 12$.

722

723 Figure 7: TEM images of the series of samples synthesized at $\text{pH}_i = 12$ for different synthesis times:
724 NT42 - 1 day (a, b); NT0 - 6 days (c, d); NT28 - 31 days (e, f); and NT33 - 183 days (g, h).

725

726 Figure 8: MIR spectra of the series of samples synthesized at $\text{pH}_i = 13.3$.

727

728 Figure 9: TEM images of the series of samples synthesized at $\text{pH}_i = 13.3$ for different synthesis
729 times: NT41 - 1 day (a, b, c); NT32 - 31 days (d, e, f); and NT35 - 183 days (g, h). (a) A = nontronite
730 particles with around 50 nm in diameter; B = nontronite particles with hundreds nm in diameter.

731

732 Figure 10: Thermodynamic stability diagrams at 150 °C of aegirine ($\text{Si}_2\text{Fe(III)NaO}_6$), hematite
733 (Fe_2O_3), ferripyrophyllite ($\text{Si}_4^{[6]}\text{Fe(III)}_2\text{O}_{10}(\text{OH})_2$), and nontronite [$\text{Si}_{4-x}^{[4]}\text{Fe(III)}_x$] $^{[6]}\text{Fe(III)}_2\text{O}_{10}$
734 $(\text{OH})_2\text{Na}_x$. (a) nontronite with $x = 0.5$ (black lines) and $x = 0.75$ (grey lines). (b) nontronite with x
735 $= 1.15$ (black lines) and $x = 1.35$ (grey lines). Black dots correspond to chemical solutions at the
736 end of experiments. The estimated errors are given by the diameter of black dots. Solubility line of
737 amorphous silica was plotted according to Gunnarsson and Arnórsson (2000).

738

739 Figure 11: Relative amounts of solid phases (arbitrary units) successively observed at different
740 times of synthesis, at 150 °C, in the Si-Fe(III)-Na system.

741

742 Figure 12: Amounts of tetrahedral iron ($^{[4]}\text{Fe(III)}$) in synthetic nontronites vs. the end of synthesis
743 pH (pH_f).

744
745 Figure 13: Thermodynamic stability diagrams at 70 °C of aegirine, hematite, ferripyrophyllite, and
746 nontronite $[\text{Si}_{3.7}^{[4]}\text{Fe(III)}_{0.3}]^{[6]}\text{Fe(III)}_2\text{O}_{10}(\text{OH})_2\text{Na}_{0.3}$. Empty circle corresponds to the chemistry
747 of the pore water core 684 in sediments of Atlantis II deep, Red Sea (Data from Blanc et al. (1986);
748 Anschulz et al., (1995, 2000)).